

# Global-Local Progressive Integration Network for Blind Image Quality Assessment

Xiaoqi Wang, Yun Zhang, *Senior Member, IEEE*

**Abstract**—Vision transformers (ViTs) excel in computer vision for modeling long-term dependencies, yet face two key challenges for image quality assessment (IQA): discarding fine details during patch embedding, and requiring extensive training data due to lack of inductive biases. In this study, we propose a Global-Local progressive INTegration network for IQA, called GlintIQA, to address these issues through three key components: 1) Hybrid feature extraction combines ViT-based global feature extractor (VGFE) and convolutional neural networks (CNNs)-based local feature extractor (CLFE) to capture global coarse-grained features and local fine-grained features, respectively. The incorporation of CNNs mitigates the patch-level information loss and inductive bias constraints inherent to ViT architectures. 2) Progressive feature integration leverages diverse kernel sizes in embedding to spatially align coarse- and fine-grained features, and progressively aggregate these features by interactively stacking channel-wise attention and spatial enhancement modules to build effective quality-aware representations. 3) Content similarity-based labeling approach is proposed that automatically assigns quality labels to images with diverse content based on subjective quality scores. This addresses the scarcity of labeled training data in synthetic datasets and bolsters model generalization. The experimental results demonstrate the efficacy of our approach, yielding 5.04% average SROCC gains on cross-authentic dataset evaluations. Moreover, our model and its counterpart pre-trained on the proposed dataset respectively exhibited 5.40% and 13.23% improvements on across-synthetic datasets evaluation<sup>1</sup>.

**Index Terms**—Blind image quality assessment, dataset construction, vision transformer, features fusion.

## I. INTRODUCTION

OBJECTIVE image quality assessment (IQA) aims to enable automated evaluation of visual image quality in alignment with human perception. IQA plays a crucial role in various image processing pipelines, such as restoration, medical imaging and retrieval, ensuring optimal visual experiences across diverse applications. IQA methods can be classified into three groups based on the availability of reference information: full-reference (FR-IQA), reduced-reference (RR-IQA), and no-reference IQA (NR-IQA) or blind IQA (BIQA) [1]. Owing to the unavailability of reference information in real-world scenarios, BIQA methods have attracted considerable attention and research efforts in the IQA domain.

Traditional BIQA methods [2]–[6] rely on hand-crafted features, such as discrete wavelet coefficients [2] and locally normalized luminance coefficients [6], for training using traditional learning algorithms, such as support vector regression

Xiaoqi Wang and Yun Zhang are with the School of Electronics and Communication Engineering, Sun Yat-sen University, Shenzhen, 518107, China (e-mail: wangxq79@mail2.sysu.edu.cn; zhangyun2@mail.sysu.edu.cn).

<sup>1</sup>The codes and proposed dataset will be released at [here](#).

(SVR) [3] and multivariate Gaussian models (MVG) [5]. However, these methods are limited by the need for extensive domain expertise and the inability to fully capture complex distortions in real-world images, affecting accuracy and generalization. In contrast, deep learning-based BIQA methods [7]–[13] leverage neural networks to learn distortion features and image quality end-to-end, demonstrating promising performance and becoming a highly sought-after research direction.

The effectiveness of deep learning-based BIQA methods depends on two critical factors: model and data. Convolutional neural networks (CNNs) are prevalent and effective tools for feature learning and representation. In the process, convolutional kernels slide across the spatial dimensions of the input images, focusing on local windows to detect visual patterns and transform the data into discriminative feature spaces. In developing CNNs-based BIQA models, quality-aware features can be learned through various distortion-related optimization paradigms, such as distortion type classification [9] and distortion strength ranking [14]. These features are then inputted into regression modules like multi-layer perceptrons (MLPs) to predict image quality scores. To improve the generalization of BIQA models trained on limited IQA databases, researchers have introduced augmentation techniques, such as patch cropping to enlarge the training set and synthesizing distorted images with varied distortion types and parameters [10].

Recently, vision Transformers (ViTs) have garnered substantial interest across diverse vision applications. Researchers have also investigated their potential in learning image quality. Generally, ViTs-based FR-IQA models [15] can achieve strong performance, benefitting from access to reference information. However, there are still two limitations associated with ViTs-based BIQA models. First, some studies leverage ViTs as regression modules to learn image quality from CNN-extracted features [16], [17]. However, such approaches inherently limit the representational capability of the CNN-extracted features that fail to fully encode long-range dependencies. Second, directly utilizing ViTs [18]–[20] as feature extraction modules may also pose challenges due to the patch embedding process, which discretizes the input image into visual tokens, where each token represents a low-resolution image patch rather than an individual pixel, leading to a loss of local fine-grained spatial details.

Moreover, despite ViTs demonstrating proficiency in capturing global dependencies, their lack of inductive biases necessitates larger datasets to achieve comparable performance [21]. However, the synthetic distortion datasets, such as [22]–[24], commonly employed for evaluating BIQA models often suffer from limited content diversity. For instance, TID2013 [23]

comprises a mere 3,000 images across 25 content types, while KADID-10k [24] offers 10,125 images with 81 content types. The development of extensive and varied IQA datasets is constrained by the high costs and complexities of subjective quality assessments, limiting ViTs' efficacy in understanding diverse image distortions. While prior works have explored data augmentation, such as using injected distortion levels or FR-IQA algorithms for quality annotation, the methods only deliver coarse information or exhibit distortion type biases [25]. Thus, it is crucial to devise more accurate labeling techniques to improve the robustness of BIQA models.

This paper addresses two critical aspects of IQA: model architecture and training data. Regarding model design, we propose a **Global-Local** progressive **INT**egration network, termed **GlintIQA**, that combines ViT and CNNs-based extractors to capture multi-grained feature representations, which are subsequently fused through channel-wise attention and spatial enhancement modules. The progressive integration approach efficiently handles diverse multi-grained features simultaneously, with each integration stage involving spatial feature enhancement and channel importance optimization to refine the resulting fused representations. Regarding training data, we exploit the correlation between content similarity and quality scores to facilitate automated labeling, which directly utilizes subjective scores to better capture the distribution of human quality perceptions. The main contributions of this paper are threefold:

- We proposed **GlintIQA** that employs a hybrid feature extraction scheme combining a ViT-based global feature extractor (VGFE) and a CNN-based local feature extractor (CLFE). This synergistic architecture effectively captures both global coarse-grained and local fine-grained features, addressing the patch-level information loss and inductive bias issues inherent in ViTs.
- We proposed an efficient feature integration strategy to handle multi-grained representations from the hybrid extractors. The strategy utilizes multiple kernel embeddings for spatial alignment, and progressively integrates fine and coarse-grained features using channel-wise attention and spatial enhancement modules.
- We proposed a content similarity-guided labeling approach that leverages the correlation between content similarity and quality scores for automated annotation of training data. This method directly incorporates subjective scores, better reflecting human perception distribution and improving annotation accuracy over techniques based on FR-IQA predictions.

The paper is structured as follows: Section **II** reviews BIQA methods regarding models and data. Section **III** details the proposed global-local integration network. Section **IV** outlines dataset construction procedures, including image degradation and label assignment. Section **V** presents extensive comparisons with existing BIQA methods across ten IQA datasets and ablation studies validating the effectiveness. Finally, Section **VI** provides a conclusion.

## II. RELATED WORK

In this section, related work on deep learning-based BIQA methods has been reviewed from both the model architecture and training data perspectives.

### A. Architecture of BIQA Models

Over the past decade, researchers have developed diverse neural networks, such as CNNs, and ViTs, as well as various architectures, such as single-stream, dual-stream, and duo-stream structures, to learn image distortion representations and regress image quality scores. CNNs have emerged as the dominant architecture for developing diverse BIQA models. Early BIQA models [7], [8], [11] primarily employed single-stream architectures, stacking CNN layers and linear layers to regress image quality scores in an end-to-end manner. To enhance assessment accuracy, researchers have designed dual-stream architectures that enable more effective feature extraction and optimized quality representation learning. For instance, Wang et al. [26] integrated distorted images with their corresponding gradient maps to augment the extraction of structural detail features. Ma et al. [9] introduced an auxiliary distortion recognition branch into the quality prediction network, accounting for the impact of diverse distortion types on image quality perception. Zhang et al. [12] presented a dual-stream architecture that integrates semantic and distortion perception, enabling adaptation to both authentic and synthetic distortion assessment scenarios. On the other hand, Liu et al. [10] employed Siamese networks to establish pairwise rankings among images exhibiting varying levels of distortion for learning the relative quality representations. To enrich feature extraction, Wu et al. [27] proposed a multi-stream structure that simultaneously extracts features from distorted images, reconstructed images, error maps, and structural degradation maps. Furthermore, Wu et al. [28] adopted hierarchical structures that employ modules across different stages of the model to capture features across diverse scales.

CNN-based BIQA models have shown significant progress, with the transition from single-stream to multi-stream and hierarchical structures demonstrating a clear trend towards richer and more robust feature extraction techniques. However, despite these advancements, CNNs' inherent local processing nature [29] can limit their capacity to model global dependencies within images. With the success of transformer models in visual tasks, several studies [16], [17], [30]–[34] have explored their application in BIQA. For instance, You et al. [17] leveraged Transformer to establish a mapping from semantic features to quality scores. Golestan et al. [16] further constrained the features to represent quality consistency under flipping and learned the relative quality ordering among images. Zhu et al. [30] introduced a saliency map within the feature space to guide the Transformer's attention towards regions of interest during the regression phase. These works have been focused on developing CNNs-based feature extractors and Transformer-based regressors. In addition, studies utilizing Transformers as feature extraction backbones has demonstrated promising results [33], [34]. Wang et al. [33] built a swin Transformer-based siamese network trained jointly

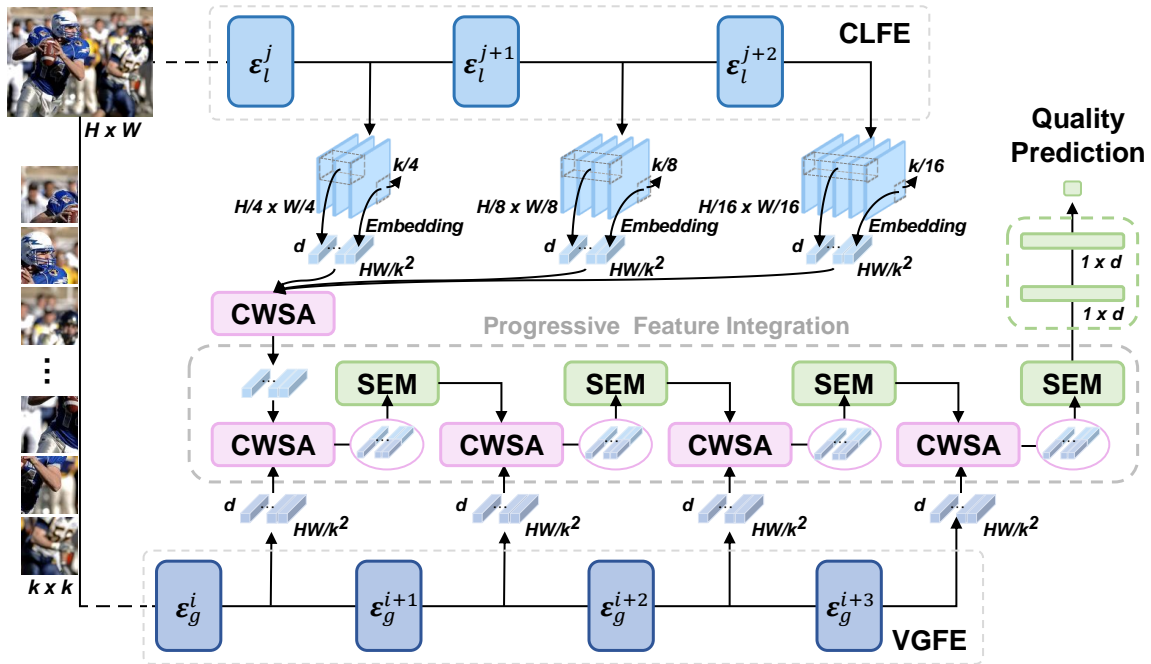


Fig. 1. The framework of the proposed GlintIQA. The input image is processed by both VGFE and CLFE for global and local feature extraction, followed by feature alignment and progressive integration through interactive stacking of CWSA and SEM. The resulting multi-grained representation is fed to an MLP for image quality prediction. For clarity, dashed lines represent omitted network layers preceding CLFE and VGFE.

on regression and pairwise ranking tasks. Qin et al. [34] proposed an attention mechanism on transformer-encoded features, mimicking diverse human evaluations for quality prediction from various perspectives. While ViTs-based backbones excel at capturing global features, the patch embedding process makes them insensitive to intra-patch details and lacks the inductive biases inherent in CNN architectures. Therefore, the development of hybrid models combining CNNs and ViTs has the potential to leverage the advantages of both architectures, offering a comprehensive feature extraction approach that addresses both local and global aspects of image quality. This hybrid strategy could mitigate the inductive biases of ViTs, resulting in more accurate and robust BIQA models.

#### B. Data Augmentation of BIQA Models

Regarding the data aspect, researchers addressed overfitting issues in size-restricted IQA databases through augmentation techniques and training strategies, including patch-based augmentation methods and pre-training with expanded datasets. The patch-based approach randomly selects image patches of varying sizes, such as  $32 \times 32$  employed in [7] or  $256 \times 256$  employed in [9], from the full images. The corresponding mean opinion scores of these patches then serve as the regression targets for model training. To mitigate potential label bias from small patches, Kim et al. [35] utilized patch-level quality scores from FR-IQA methods as intermediate regression targets. Furthermore, several studies [9], [10], [27], [28], [36] created large-scale datasets for pre-training BIQA models. For instance, Ma et al. [9] synthesized images with different distortions using artificial degradation for training distortion classification networks. Liu et al. [10] leveraged injected distortion levels of synthetic images as quality rankings.

Ma et al. [27] and Gu et al. [36] calculated quality scores for a large number of synthetically distorted images using either a single FR-IQA method [37] or by fusing the results of multiple FR-IQA methods in [28].

Previous work has explored data augmentation strategies for synthetic distortions, using injected distortion levels as quality labels or FR-IQA algorithms for quality annotation. However, these methods have inherent shortcomings. Distortion level labels can only partially reflect image quality that cannot capture the continuous degradation of image quality. Although FR-IQA algorithms can generate fine-grained image quality scores, they may exhibit biases towards certain distortion types. For instance, while Peak Signal-to-Noise Ratio (PSNR) adequately estimates images corrupted by additive noise and quantization artifacts, it falls short in assessing numerous other distortion types [25]. In addition, these FR-IQA algorithms often rely on low-level feature discrepancies to quantify distortion severity, overlooking the significant role of high-level semantic content in visual quality perception.

### III. THE PROPOSED GLINTIQA

As illustrated in Fig. 1, the proposed GlintIQA first leverages a hybrid feature extraction scheme combining ViT-based global feature extractor and CNNs-based local feature extractor, which respectively leverages ViT for capturing global coarse-grained features and CNNs for extracting fine-grained details at multiple scales. Then, interactive stacks of channel-wise attention and local spatial enhancement modules progressively integrate these features to build multi-grained representations. The integrated multi-grained features are finally passed through an MLP to generate the perceptual image quality score.

### A. Global and Local Feature Extraction

1) *ViT-based Global feature extractor (VGFE)*: Global features are indispensable for image quality evaluation, providing holistic contextual information. While convolutional operations focus on local features, the VGFE utilizes the power of self-attention mechanisms to capture long-range relationships between image regions. We utilize four vision Transformer blocks [18], where  $i$ -th block denote as  $\mathcal{E}_g^i$  with parameters  $\omega_g^j$ . Given an image  $\mathbf{x} \in \mathbb{R}^{3 \times H \times W}$ , the image is partitioned into non-overlapping patches that precede global dependency modeling. Subsequently, a patch embedding layer maps these patches to individual tokens, typically achieved through convolution and flatten operation, which can be represented as:

$$\mathbf{f}_g^e = \psi_f \left( \varphi_{conv(3, d, k)} (\mathbf{x}) \right)^T, \quad (1)$$

where the notation  $\varphi_{conv(3, d, k)}$  represents a 2D convolutional layer with convolutional kernel size and stride of  $k$  that embeds the input image with 3 channels into a feature space of  $d$  dimensions. The function  $\psi_f$  represents the flattening operation that collapses the output of the convolutional layer along the spatial dimensions, yielding  $\mathbf{f}_g^e \in \mathbb{R}^{d \times \frac{HW}{k^2}}$ . Subsequently,  $\mathbf{f}_g^e$  is transposed to obtain features within  $\mathbb{R}^{\frac{HW}{k^2} \times d}$ , where each patch of size  $k \times k$  is represented by a vector of length  $d$ , referred to as a token. For simplicity, we have omitted the description of the class token and positional embedding used in the original ViT architecture.

Subsequently, these tokens are input into a Transformer block for extracting global features. The output of the  $i$ -th block can be expressed as:

$$\mathbf{f}_g^i = \mathcal{E}_g^i (\mathbf{x}; \omega_g^i), \quad (2)$$

where the extracted features at different scales maintain consistent dimensionality, residing in  $\mathbb{R}^{\frac{HW}{k^2} \times d}$ .

Although the patch embedding process, as shown in Eq. 1, enables subsequent models to capture global context, it may result in the loss of fine-grained details within patches. As shown in Fig. 2(a), patch embedding discretizes the input image into a sequence of visual tokens, significantly reducing spatial dimensions in a single step at the model input. This discretization inevitably leads to a loss of fine-grained details and local spatial information, as the individual tokens correspond to low-resolution patches rather than individual pixels. To address this limitation, we exploit a local feature extractor consisting of a series of convolutional layers, as depicted in Fig. 2(b). This extractor uses small convolutional kernels and strides to progressively reduce the dimensions of the image, which can preserve certain local image details in the extracted features. Moreover, the integrated CNNs-based structure can mitigate the inherent lack of inductive bias in ViT. By leveraging the strengths of both CNNs and ViTs, the hybrid model effectively captures both global and local features, ensuring a more accurate and robust representation of image quality.

2) *CNNs-based Local feature extractor (CLFE)*: Local features, such as edges and textures, reside within small image regions and provide valuable insights into the nature and severity of local distortions. To meticulously extract these features,

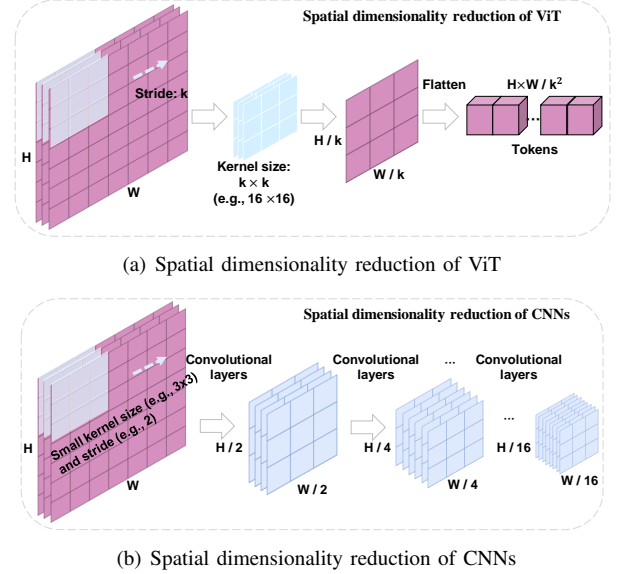


Fig. 2. Comparison of spatial dimensionality reduction in ViT and CNNs. (a): In ViT, the spatial dimensionality reduction occurs through the patch embedding process, which subdivides an input image of dimensions  $H \times W$  into non-overlapping patches using a convolutional layer with a kernel size  $k \times k$  and stride  $k$  (e.g.,  $k = 16$ ), resulting in tokens of size  $H/k \times W/k$ . (b): Spatial dimensionality reduction in CNNs involves applying successive convolutional layers with small kernel sizes (e.g.,  $3 \times 3$ ) and strides (e.g., 2), progressively halving the spatial dimension.

the CLFE utilizes three residual blocks from ResNet50 [38], denoted as  $\mathcal{E}_l^j$  with parameters  $\omega_l^j$ , where  $j$  represents the index of the blocks. Each block yields features at distinct scales, downsampled by factors of  $2^{j+1}$  relative to the original image.

To ensure the local and global features are aligned in size before further integration, a multi-kernel embedding scheme is employed that adjusts the kernel size and stride based on the downsampling ratio of the input features. Specifically, the processing of the  $j$ -th output feature can be represented as:

$$\mathbf{f}_l^j = \psi_f \left( \varphi_{conv(c_j, d, k/2^{j+1})} \left( \mathcal{E}_l^j (\mathbf{x}; \omega_l^j) \right) \right)^T, \quad (3)$$

where  $c_j$  denotes the feature channels of the output from the  $j$ -th residual block. To maintain spatial alignment of features at the  $j$ -th level, which has undergone a  $2^{j+1}$ -fold reduction in size, convolutional kernels and strides are adaptively set to  $k/2^{j+1}$ , ensuring precise correspondence with the original image region dimensions of  $k \times k$ .

The outputs of the three side blocks are concatenated along the channel dimension. Then, we model the channel weights for multi-scale features through channel-wise self-attention. Following this, a linear layer is utilized to map these features to a dimensionality of  $d$ . These processes can be represented as:

$$\mathbf{f}_l = \varphi_{p(3d, d)} \left( \mathcal{M}_{CWSA} \left( \mathbf{f}_l^{j-1} \oplus \mathbf{f}_l^j \oplus \mathbf{f}_l^{j+1} \right) \right), \quad (4)$$

where  $\mathbf{f}_l \in \mathbb{R}^{\frac{HW}{k^2} \times d}$  and  $\oplus$  denotes a concatenation operation, and  $\varphi_{p(3d, d)}$  denotes a linear projection layer with input and output dimensions of  $3d$  and  $d$ , respectively. The CWSA module, denoted as  $\mathcal{M}_{CWSA}$ , is described in detail in the following subsection.

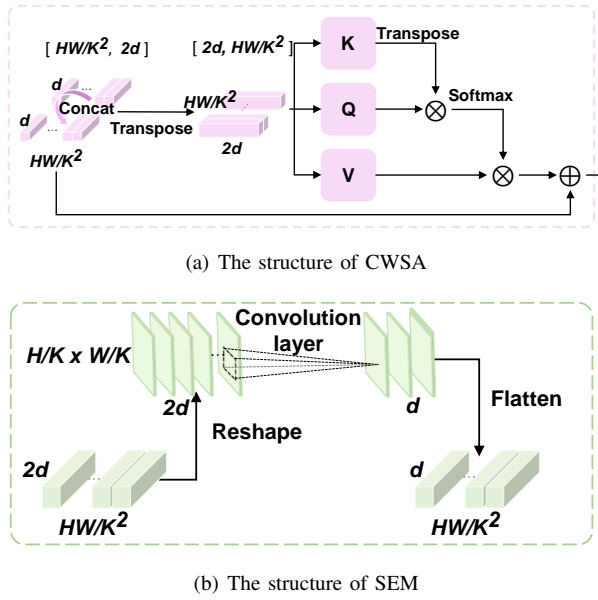


Fig. 3. Structures of (a) channel-wise Self-attention (CWSA) and (b) Spatial Enhancement Module (SEM).

### B. Local and Global Feature Integration

1) *Progressive Feature Integration*: Directly concatenating and fusing features at multiple granularities may pose challenges for the model to handle diverse information simultaneously. Therefore, we adopt a progressive approach to integrate features layer by layer while optimizing the channel and spatial representations of the fused features. Specifically, we start by concatenating the fine-grained feature  $\mathbf{f}_l$  with the coarse-grained global feature at the initial scale. Then, a stacked combination of CWSA and a SEM is used to progressively fuse features in a hierarchical manner. The feature integration process can be concisely represented as:

$$\begin{aligned} \mathbf{z}_i &= (\mathbf{f}_i \oplus \mathbf{f}_g)^T; \\ \hat{\mathbf{z}}_i &= \mathcal{M}_{\text{CWSA}}(\mathbf{z}_i); \\ \mathbf{f}_{i+1} &= \mathcal{M}_{\text{SEM}}(\hat{\mathbf{z}}_i). \end{aligned} \quad (5)$$

For  $i = 1$ ,  $\mathbf{f}_i$  represents the output feature of the CLFE, i.e.,  $\mathbf{f}_l$ . For other values of  $i$ ,  $\mathbf{f}_i$  is the output feature of the SEM, denoted as  $\mathcal{M}_{\text{SEM}}$ .

2) *Channel-wise Self-attention (CWSA)*: This module is designed to learn the importance of different channels in features (extracted by CNNs and ViTs). By accurately weighting these channels, the model can emphasize the most informative features [39], leading to improved overall performance. As illustrated in Fig. 3(a), CWSA concatenates two inputs to obtain the feature  $\mathbf{z}_i$  as shown in Eq. 5. Subsequently, the feature is transposed and subjected to a self-attention computation. Specifically,  $\mathbf{z}_i$  is projected into three representations for query, key, and value through three distinct linear layers, which is expressed as:

$$\mathbf{Q} = \varphi_{p(d,d)}^Q(\mathbf{z}_i); \mathbf{K} = \varphi_{p(d,d)}^K(\mathbf{z}_i); \mathbf{V} = \varphi_{p(d,d)}^V(\mathbf{z}_i). \quad (6)$$

The softmax scores quantify the channel-wise significance, which get applied to the scaled dot product of queries ( $\mathbf{Q}$ )

and keys ( $\mathbf{K}$ ), normalized by  $\sqrt{d}$  ( $d$  being the dimension). The CWSA output is the weighted summation of values ( $\mathbf{V}$ ) based on these attention scores, combined with the previous input feature  $\mathbf{z}_i$ , which is expressed as:

$$\hat{\mathbf{z}}_i = \varphi_{\text{Softmax}}(\mathbf{Q} \cdot \mathbf{K}^T / \sqrt{d}) \cdot \mathbf{V} + \mathbf{z}_i. \quad (7)$$

3) *Spatial Enhancement Module (SEM)*: Following the CWSA module, we introduce SEM to enhance the interaction of features extracted by CNNs and ViT. The SEM reshapes and applies convolutional operations to the tokens for the input tensor  $\hat{\mathbf{z}}_i$ , as illustrated in Fig. 3(b). The computational process is expressed as:

$$\mathbf{f}_{i+1} = \psi_f(\varphi_{\text{conv}}(2d, d, 3)(\psi_r(\hat{\mathbf{z}}_i))), \quad (8)$$

where the notation  $\psi_r$  indicates the operation of reshaping the token vectors into 2D feature maps. The convolutional layer  $\varphi_{\text{conv}}(2d, d, 3)$  employs a  $3 \times 3$  filter with a stride of 1. Finally, the output of the convolutional layer is reshaped back to a flattened tensor, aligning it with the original input dimensions.

### C. Image Quality Prediction

The quality score prediction is performed via an MLP architecture, which consists of two linear layers interspersed with GELU activation function and dropout layers for regularization. Specifically, the feature map output from the SEM module is denoted as  $\mathbf{f}$ . To generalize the global distribution of these features and obtain a concise quality representation, feature  $\mathbf{f}_5$  is spatially averaged to form a  $d$ -dimensional vector  $\hat{\mathbf{f}} \in \mathbb{R}^{1 \times d}$ . This is fed into the MLP to generate a prediction score  $s$ , which can be represented as:

$$s = \varphi_{p(d,1)}\left(\varphi_{p(d,d)}(\hat{\mathbf{f}})\right). \quad (9)$$

For simplicity, the specific details of the activation function and dropout layer are omitted from the above equation. Ultimately,  $l_1$  loss function is utilized to enable end-to-end model parameter updates.

## IV. THE PROPOSED CONTENT SIMILARITY-GUIDED LABELING METHOD

Deep neural networks typically possess a large number of learnable parameters, necessitating access to large-scale and diverse training datasets to facilitate effective learning and achieve better generalization capability. However, synthetic distortion datasets often lack content diversity, necessitating effective data augmentation. Patch-based augmentation method, while expanding the training set, introduces labeling biases that hinder performance improvements. Furthermore, FR-IQA-labeled data may suffer from prediction biases for specific distortion types and fail to capture high-level semantic impacts on quality. To address these limitations, this section introduces a novel annotation strategy based on quality label transfer using content similarity. We first evaluate the effectiveness of this approach in automatically annotating image quality, followed by a detailed explanation of the construction process for a large-scale synthetic distortion dataset.

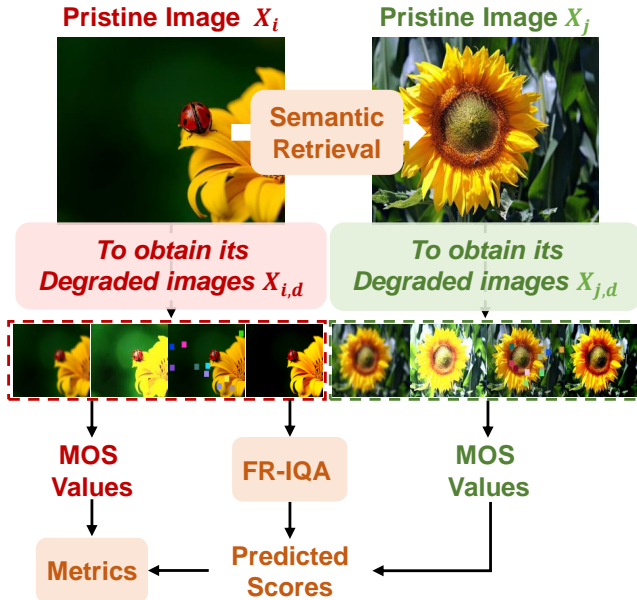


Fig. 4. Analyzing workflow of correlation between image content similarity and visual perception quality.

#### A. MOS Correlation Analysis for Semantically Similar Images

The proposed labeling method draws inspiration from empirical findings that images with similar content tend to have comparable visual quality when degraded by the same type and level of distortion [40]. To further substantiate the viability of this method, we conduct an analysis of an example using the KADID-10k [24] as shown in Fig. 4. Specifically, given a pristine image  $X_i$  and its corresponding distorted images  $\mathbf{X}_{i,d} = \{x_{i,d}^{1,1}, \dots, x_{i,d}^{k,l}\}$ , where  $k$  and  $l$  respectively represent the  $k$ -th type and  $l$ -th level of distortion, we utilize semantic feature vector to represent the image content. Then, a pristine image  $X_j$  with similar content to  $X_i$  was retrieved using cosine similarity between semantic vectors. The MOS values of distorted images  $\mathbf{X}_{j,d}$  from KADID-10k were then used as predicted quality scores for  $X_{i,d}$ . To benchmark this evaluation, we analyzed the results for all pristine images in KADID-10k and compared it against several FR-IQA algorithms, i.e., SSIM [41], FSIMc [42], and VSI [37]. As illustrated in Fig. 5, our method outperforms these FR-IQA algorithms in the majority of cases, as evidenced by the SROCC and RMSE metrics. In a comprehensive evaluation of 81 distorted image sets, our method achieved the best SROCC in 88.9% (72 of the sets) and the best RMSE in 86.4% (70 of the sets), which demonstrate superior correlation and accuracy values, respectively. Hence, images with similar content exhibit similar visual quality labels under identical or similar distortion conditions. Based on this idea, the proposed approach involves leveraging human-annotated images to identify content-similar images, applying the same distortions, and subsequently transferring the annotations. Next, we describe the specific steps for constructing the proposed content similarity-guided dataset.

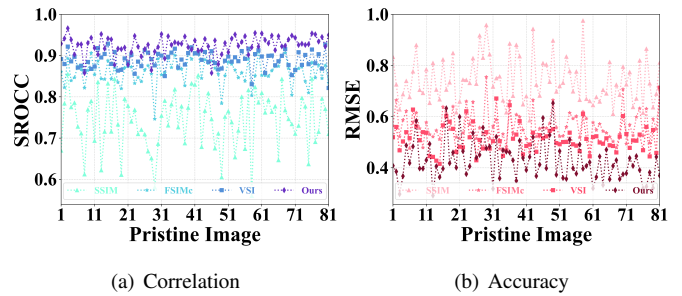


Fig. 5. The results of our labeling method. Our labeling method achieved superior performance compared to these FR-IQA methods in the majority of cases for correlation and accuracy metrics, when evaluating distorted versions of 81 pristine images in KADID-10k.

#### B. Dataset Construction

1) *Preliminary*.: To create the dataset, we selected 50,000 high-quality images from KADIS-700k [24] and applied 25 types of distortions with five intensity levels to each image. The distortion types were selected to be consistent with those present in KADID-10k [24]. Finally, this process produced 6,250,000 degraded images.

The quality of the generated images was annotated using MOS values obtained from an IQA database, i.e., KADID-10k, where the IQA database with  $P$  pristine images is denoted as  $\{(\mathbf{X}_{i,d}, \mathbf{M}_{i,d})\}_{i=1}^P$ . The set  $\mathbf{X}_{i,d} = \{x_{i,d}^{1,1}, \dots, x_{i,d}^{k,l}\}$  represents the degraded images of the  $i$ -th pristine image  $X_i$ , and  $\mathbf{M}_{i,d} = \{m_{i,d}^{1,1}, \dots, m_{i,d}^{k,l}\}$  contains their corresponding MOS values, which were normalized using min-max scaling and mapped to a scale ranging from 0 to 9. Each degraded image  $x_{i,d}^{k,l}$  corresponds to a pristine image  $X_i$  degraded with the  $k$ -th type at the  $l$ -th level of distortion, with its MOS value given by  $m_{i,d}^{k,l}$ . The high-quality images are represented as a set denoted by  $\{I_j\}_{j=1}^H$ , where  $I_j$  and  $H$  refer to the  $j$ -th high-quality image and the total number of images, respectively.

2) *Dataset construction*.: The process of constructing the dataset is shown in Fig. 6. To start the process, the first objective is to retrieve a pristine image  $X_i$  that exhibits similar content to a given image  $I_j$ . To achieve this, we extract the semantic feature vectors of  $X_i$  and  $I_j$  using ResNet101 [38] without the final linear layer, where these semantic vectors denote as  $\mathbf{v}_i$  and  $\mathbf{v}_j \in \mathbb{R}^{1 \times 2048}$ , respectively. Following that, the similarity between their image contents is assessed by calculating the cosine similarity between their semantic features. The most similar pristine image is identified by:

$$\hat{i} = \underset{i \in \{1, \dots, P\}}{\operatorname{argmax}} \cos(\mathbf{v}_i, \mathbf{v}_j) = \frac{\mathbf{v}_i \cdot \mathbf{v}_j^T}{\|\mathbf{v}_i\| \cdot \|\mathbf{v}_j\|}. \quad (10)$$

In the second step, based on the retrieved pristine image  $X_i$ , we obtain corresponding distorted images  $\mathbf{X}_{i,d}$  and MOS values  $\mathbf{M}_{i,d}$  from IQA database. The third step involves degrading  $I_j$  using the same type and level of distortion as applied to the pristine image  $X_i$ . This degradation process is represented by an operation  $W_i^{k,l}(\cdot)$  that generates a degraded image denoted as  $I_{j,d}^{k,l}$ <sup>2</sup>. In the fourth step, the MOS value  $m_{i,d}^{k,l}$

<sup>2</sup>The synthetic distortion procedure available at: [here](#).

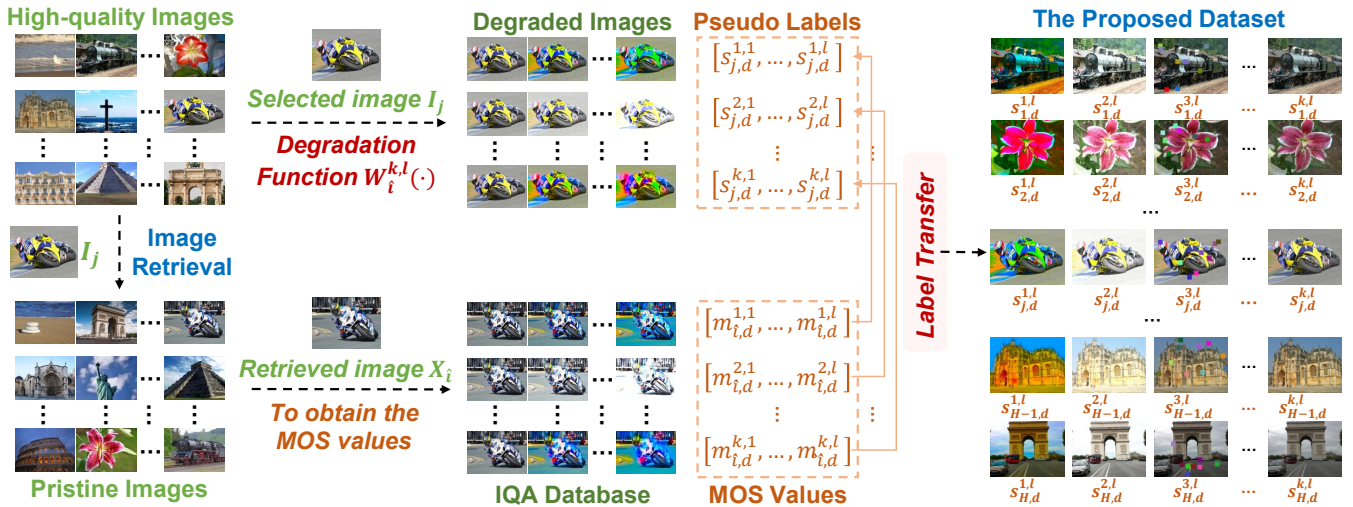


Fig. 6. The scheme of the proposed content similarity-guided labeling method.

corresponding to  $x_{i,d}^{k,l}$  is used to annotate the degraded image  $I_{j,d}^{k,l}$ . The generation of degraded images and the labeling process can be described as

$$\left\{ (I_{j,d}^{k,l}, s_{j,d}^{k,l}) \mid I_{j,d}^{k,l} = W_i^{k,l}(I_j), s_{j,d}^{k,l} = m_{i,d}^{k,l}, 1 \leq j \leq H \right\}. \quad (11)$$

Finally, the generated dataset can be represented as  $\{(\mathbf{I}_{j,d}, \mathbf{S}_{j,d})\}_{j=1}^H$ , where  $\mathbf{I}_{j,d} = \{I_{j,d}^{1,1}, \dots, I_{j,d}^{k,l}\}$  and  $\mathbf{S}_{j,d} = \{s_{j,d}^{1,1}, \dots, s_{j,d}^{k,l}\}$ . The proposed content-guided label transfer method generates quality scores closely aligning with the true distribution of subjective opinion scores, as labels derive from genuine human annotations. Moreover, the proposed approach considers image content influence on quality perception in a content-driven manner. In contrast, the FR-IQA approach hardly captures high-level semantics, and its labels ignore the impact of content perception on quality assessment.

## V. EXPERIMENT

This section first presents the experimental setting covering databases, protocols, and implementation details. After that, the experimental results are compared to state-of-the-art BIQA methods on ten IQA databases. Finally, we conducted comprehensive ablation studies to further analyze the effectiveness of our approach. thoroughly analyze the effectiveness of our approach.

### A. Experimental Settings

1) *Databases and protocols*: A comprehensive evaluation of the proposed model was conducted across ten IQA benchmark databases for IQA, including five synthetic distortion datasets, specifically LIVE [22], CSIQ [43], TID2013 [23], KADID-10k [24], and LIVE-MD [44], alongside five authentic distortion datasets, namely BID [45], CLIVE [46], KonIQ-10k [47], SPAQ [48], and LIVEFB [49]. Within the synthetic distortion datasets, the LIVE-MD dataset features images with multiple distortion types, whereas the remaining databases primarily focus on images with a single distortion type.

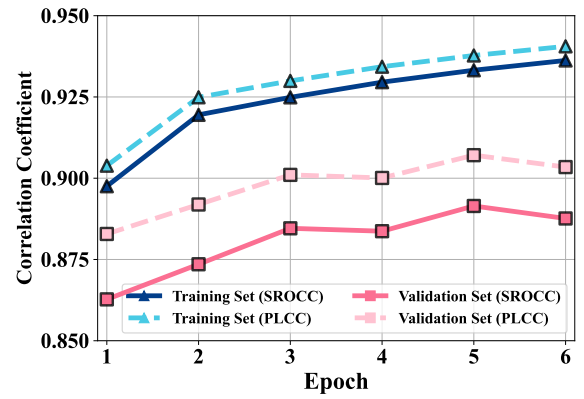


Fig. 7. The pre-training results of the proposed dataset.

Synthetic distortion datasets are constructed by algorithmically degrading original images, resulting in minimized content variation but a wide range of artificial distortions. In contrast, authentic distortion datasets comprise images captured in real-world settings, exhibiting substantial content diversity from varied scenes, objects and conditions encountered. The details of sample size, image resolution, and label types for each database are summarized in Table I.

The evaluation of BIQA methods employs two widely-adopted correlation metrics: Spearman's rank-order correlation coefficient (SROCC) and Pearson's linear correlation coefficient (PLCC). SROCC quantifies the monotonic association between predicted scores and ground truth, while PLCC measures their linear relationship. Specifically, SROCC computes the squared disparity between the ranks of predicted quality scores and MOS values. On the other hand, PLCC quantifies linear relationship between predicted quality scores and MOS values by calculating the covariance divided by the product of their standard deviations.

2) *Implementation details*: The proposed model was implemented using the PyTorch framework and evaluated on

TABLE I  
COMPREHENSIVE SUMMARY OF IQA DATABASES FOR BENCHMARKING BIQA MODELS.

| Database       | Ref. Image Count | Dist. Type Count | Dist. Image Count | Image Resolution                         | Label Type | Database Type |
|----------------|------------------|------------------|-------------------|--|------------|---------------|
| LIVE [22]      | 29               | 5                | 779               | $480 \times 720 \sim 768 \times 512$     | DMOS       | Synthetic     |
| CSIQ [43]      | 30               | 6                | 866               | $512 \times 512$                         | DMOS       | Synthetic     |
| TID2013 [23]   | 25               | 24               | 3,000             | $384 \times 512$                         | MOS        | Synthetic     |
| KADID-10k [24] | 81               | 25               | 10,125            | $384 \times 512$                         | MOS        | Synthetic     |
| LIVE-MD [44]   | 15               | 2                | 150               | $720 \times 1280$                        | DMOS       | Synthetic     |
| BID [45]       | -                | -                | 585               | $960 \times 1280 \sim 1704 \times 2272$  | MOS        | Authentic     |
| LIVEC [46]     | -                | -                | 1,162             | $500 \times 500 \sim 640 \times 960$     | MOS        | Authentic     |
| KonIQ-10k [47] | -                | -                | 10,073            | $384 \times 512/768 \times 1024$         | MOS        | Authentic     |
| SPAQ [48]      | -                | -                | 11,125            | $1080 \times 1440 \sim 6556 \times 3744$ | MOS        | Authentic     |
| LIVEFB [49]    | -                | -                | 39,810            | $160 \times 186 \sim 660 \times 1200$    | MOS        | Authentic     |

IQA databases utilizing NVIDIA RTX 3090 GPUs. To extract local fine-grained features, we employed the first three residual blocks of ResNet50, as the early stages effectively capture local details and intricate patterns of the input image, where these blocks have 256, 512, and 1024 output channels respectively. For global feature extraction, we used four transformer blocks from ViT-S/16 [18], specifically blocks 6, 7, 8, and 9, which output 384-dimensional feature representations. The parameter  $d$  was set to 384. The CLFE and VGFE modules were initialized using pre-trained weights from ImageNet, with the initial layers frozen to mitigate rapid overfitting. The Adam optimizer with a weight decay of 1e-5 was used for training. The training process spanned 300 epochs, using a batch size of 32 and an initial learning rate of 1e-5, which was controlled by a cosine annealing schedule. In training phase, data augmentation involved randomly cropping  $224 \times 224$  pixel patches from images as input to the model. Model performance was periodically evaluated every 5 epochs. For inference, 25 randomly extracted patches of  $224 \times 224$  pixels from each test image were used to compute the final quality score by averaging their predicted scores.

Pre-training on our proposed large-scale dataset was performed using an NVIDIA A800 GPU and the Adam optimizer with 1e-5 weight decay. Due to the vast size of the dataset, the training process consists of 6 epoch, with batch size and initial learning rate set to 192 and 5e-5, respectively. The learning rate was decayed via cosine annealing scheduler for convergence. Each image was randomly cropped to  $224 \times 224$  pixels during pre-training. For validation, 1,000 images were randomly sampled from a pool of 50,000, with their corresponding degraded versions forming the validation set. To evaluate the test images, we randomly selected 10 patches and averaged their scores to yield a final prediction. Weights demonstrating optimal validation performance were retained. Training and validation results are presented in Fig. 7.

#### B. Comparison with BIQA Methods on Individual Databases

To evaluate the proposed method, we conducted experiments on five authentic and five synthetic distortions datasets. For synthetic distortion datasets, pristine images were ran-

domly partitioned into two subsets at an 8:2 ratio, with respective distorted images forming training and test sets to avoid content overlap. The authentic distortion dataset was partitioned into training and test sets in an 8:2 ratio. This process was repeated ten times with different random partitions, and the median SROCC and PLCC values were reported. As detailed in Tables II and III, we benchmarked our method against nine existing deep learning-based BIQA approaches, on both authentic and synthetic datasets. The results of the deep learning-based models were evaluated using the reported results in the original papers or replicated using their publicly released code.

1) *Authentic database evaluation:* As shown in Table II, the proposed GlintIQA demonstrates consistently superior performance across five authentic distortion datasets, achieving an average SROCC of 0.840 and PLCC of 0.867. This represents improvements of 1.94% and 1.40% over TempQT, and 0.60% and 0.46% over DEIQT, respectively. Specifically, on the CLIVE, GlintIQA achieves best results, outperforming DEIQT by 1.83% in SROCC and 1.45% in PLCC. Similarly, for the KonIQ-10k, the proposed method achieves the highest performance, with SROCC and PLCC gains of 1.63% and 1.28% over the second-best method. In the BID and SPAQ datasets, both GlintIQA and DEIQT reach best performance, with our method exhibiting a superior PLCC. Additionally, GlintIQA secures competitive results on the LIVEFB. Overall, the proposed GlintIQA exhibits superior and more stable performance compared to existing BIQA methods. The improvement of GlintIQA can be attributed to two key design elements: firstly, the method integrates both global coarse- and local fine-grained image features, enhancing its sensitivity to various distortions. Secondly, the inclusion of CNNs, specifically CLFE and SEM, significantly augments the model's inductive capacity to learn representations of different distortions. This enhanced inductive capability is particularly advantageous for achieving superior performance on smaller datasets such as CLIVE and BID.

2) *Synthetic database evaluation:* Table III summarizes the performance of BIQA models on five synthetic distortion datasets. The final two columns present the average perfor-

TABLE II

BENCHMARKING PERFORMANCE AGAINST EXISTING BIQA MODELS ON AUTHENTIC DISTORTION DATABASES, WHERE THE BEST AND SECOND-BEST PERFORMANCES ARE INDICATED BY **BLACK** BOLDED AND **GRAY** BOLDED ENTRIES, RESPECTIVELY.

| Method          | CLIVE [46]   |              | KonIQ-10k [47] |              | BID [45]     |              | SPAQ [48]    |              | LIVEFB [49]  |              | Average      |              |
|-----------------|--------------|--------------|----------------|--------------|--------------|--------------|--------------|--------------|--------------|--------------|--------------|--------------|
|                 | SROCC        | PLCC         | SROCC          | PLCC         | SROCC        | PLCC         | SROCC        | PLCC         | SROCC        | PLCC         | SROCC        | PLCC         |
| WaDIQaM-NR [11] | 0.692        | 0.730        | 0.729          | 0.754        | 0.653        | 0.636        | 0.840        | 0.845        | 0.435        | 0.430        | 0.670        | 0.679        |
| SFA [50]        | 0.812        | 0.833        | 0.856          | 0.872        | 0.826        | 0.840        | 0.906        | 0.907        | 0.542        | 0.626        | 0.788        | 0.816        |
| MUSIQ [51]      | 0.702        | 0.746        | 0.916          | 0.928        | -            | -            | <b>0.918</b> | 0.921        | -            | -            | -            | -            |
| DB-CNN [12]     | 0.844        | 0.862        | 0.878          | 0.887        | 0.845        | 0.859        | 0.910        | 0.913        | 0.554        | 0.652        | 0.806        | 0.835        |
| HyperIQA [13]   | 0.859        | 0.882        | 0.906          | 0.917        | 0.869        | 0.878        | 0.911        | 0.915        | 0.544        | 0.602        | 0.818        | 0.839        |
| TReS [16]       | 0.846        | 0.877        | 0.915          | 0.928        | 0.855        | 0.871        | 0.917        | 0.913        | 0.554        | 0.625        | 0.817        | 0.843        |
| REQA [31]       | 0.865        | 0.880        | 0.904          | 0.916        | <b>0.874</b> | 0.886        | -            | -            | -            | -            | -            | -            |
| TempQT [52]     | 0.870        | 0.886        | 0.903          | 0.920        | 0.868        | 0.902        | 0.916        | 0.922        | 0.561        | 0.646        | 0.824        | 0.855        |
| DEIQT [34]      | <b>0.875</b> | <b>0.894</b> | <b>0.921</b>   | <b>0.934</b> | <b>0.889</b> | <b>0.903</b> | <b>0.919</b> | <b>0.923</b> | <b>0.571</b> | <b>0.663</b> | <b>0.835</b> | <b>0.863</b> |
| GlintIQA        | <b>0.891</b> | <b>0.907</b> | <b>0.936</b>   | <b>0.946</b> | <b>0.889</b> | <b>0.906</b> | <b>0.919</b> | <b>0.924</b> | <b>0.566</b> | <b>0.653</b> | <b>0.840</b> | <b>0.867</b> |

TABLE III

COMPARISON TO STATE-OF-THE-ART BIQA MODELS ON FIVE SYNTHETIC IQA DATABASES, WHERE THE BEST AND SECOND-BEST PERFORMANCES ARE INDICATED BY **BLACK** BOLDED AND **GRAY** BOLDED ENTRIES, RESPECTIVELY. GLINTIQA\* WAS FINE-TUNED ON THE RESPECTIVE DATASET USING THE PRE-TRAINED MODEL ON THE PROPOSED DATASET.

| Method        | LIVE [22]    |              | CSIQ [43]    |              | TID2013 [23] |              | KADID-10k [24] |              | LIVEMD [44]  |              | Average (w/o KADID-10k) |              |
|---------------|--------------|--------------|--------------|--------------|--------------|--------------|----------------|--------------|--------------|--------------|-------------------------|--------------|
|               | SROCC        | PLCC         | SROCC        | PLCC         | SROCC        | PLCC         | SROCC          | PLCC         | SROCC        | PLCC         | SROCC                   | PLCC         |
| MEON [9]      | 0.951        | 0.955        | 0.852        | 0.864        | 0.808        | 0.824        | 0.604          | 0.691        | 0.924        | 0.940        | 0.884                   | 0.896        |
| SGDNet [53]   | 0.969        | 0.965        | 0.883        | 0.903        | 0.843        | 0.861        | -              | -            | -            | -            | -                       | -            |
| CaHDC [28]    | 0.965        | 0.964        | 0.903        | 0.914        | 0.862        | 0.878        | -              | -            | 0.927        | <b>0.950</b> | -                       | -            |
| HyperIQA [13] | 0.962        | 0.966        | 0.923        | 0.942        | 0.840        | 0.858        | 0.852          | 0.845        | <b>0.939</b> | 0.938        | 0.916                   | 0.926        |
| DB-CNN [12]   | 0.968        | 0.971        | 0.946        | 0.959        | 0.816        | 0.865        | 0.851          | 0.856        | 0.927        | 0.934        | 0.914                   | 0.932        |
| TReS [16]     | 0.969        | 0.968        | 0.922        | 0.942        | 0.863        | 0.883        | 0.859          | 0.858        | 0.930        | 0.932        | 0.921                   | 0.931        |
| AIGQA [27]    | 0.960        | 0.957        | 0.927        | 0.952        | 0.871        | 0.893        | 0.864          | 0.863        | 0.933        | <b>0.947</b> | 0.923                   | 0.937        |
| TempQT [52]   | <b>0.976</b> | 0.977        | <b>0.950</b> | 0.960        | 0.883        | 0.906        | -              | -            | 0.933        | 0.939        | <b>0.936</b>            | <b>0.946</b> |
| DEIQT [34]    | <b>0.980</b> | <b>0.982</b> | 0.946        | <b>0.963</b> | <b>0.892</b> | <b>0.908</b> | <b>0.889</b>   | <b>0.887</b> | 0.907        | 0.930        | 0.931                   | <b>0.946</b> |
| GlintIQA      | <b>0.976</b> | <b>0.980</b> | 0.941        | 0.947        | 0.857        | 0.883        | <b>0.906</b>   | <b>0.903</b> | <b>0.942</b> | 0.940        | 0.929                   | 0.938        |
| GlintIQA*     | <b>0.976</b> | 0.978        | <b>0.970</b> | <b>0.974</b> | <b>0.917</b> | <b>0.929</b> | -              | -            | 0.935        | 0.945        | <b>0.950</b>            | <b>0.957</b> |

formance across four of these datasets, excluding KADID-10k. GlintIQA\* was fine-tuned on each dataset using a model pre-trained on our proposed dataset. The proposed GlintIQA\* achieves the highest average SROCC and PLCC. Specifically, on the LIVE, most BIQA methods perform well, with GlintIQA achieving SROCC and PLCC values close to those of the top-performing DEIQT. For KADID-10k, GlintIQA surpasses DEIQT by 1.91% in SROCC and 1.80% in PLCC. GlintIQA attains the highest SROCC on LIVEMD and competitive results on CSIQ. Its performance on TID2013 is slightly lower than that of some methods, as the limited number of original images and the diversity of distortion types introduce variability in the results. However, the pre-trained GlintIQA\* shows significant improvements on CSIQ and TID2013, with SROCC and PLCC gains of 3.08% and 2.85% on CSIQ, and 7.00% and 5.21% on TID2013 compared to GlintIQA. On LIVE, GlintIQA already demonstrates high performance, leaving little room for pre-training improvement. LIVEMD includes compound distortions, while the pre-trained model is based on the proposed dataset with single distortions, resulting in minimal pre-training gains on this dataset.

In addition, the GlintIQA\* pre-trained on the proposed dataset outperforms data augmentation methods using FR-IQA annotations (CaHDC and AIGQA), as well as distortion classification-based data augmentation (DB-CNN). This demonstrates the efficacy of the proposed dataset. Furthermore, the proposed dataset can effectively enhance the gener-

TABLE IV  
SUMMARY OF THE STATISTICAL PERFORMANCE OF THE PROPOSED METHOD AND EXISTING BIQA METHODS.

| Significance test results for authentic distortion datasets. |       |           |     |      |        |
|--|-------|-----------|-----|------|--------|
|  | CLIVE | KonIQ-10k | BID | SPAQ | LIVEFB |
| DB-CNN [12]  | 1     | 1         | 1   | 1    | 1      |
| HyperIQA [13]  | 1     | 1         | 1   | 1    | 1      |
| TReS [16]  | 1     | 1         | 1   | 1    | 1      |
| TempQT [52]  | 1     | 1         | 1   | -    | 1      |
| DEIQT [34]   | 1     | 1         | -   | -    | 0      |

| Significance test results for synthetic distortion datasets. |      |      |         |           |        |
|--|------|------|---------|-----------|--------|
|  | LIVE | CSIQ | TID2013 | KADID-10k | LIVEMD |
| DB-CNN [12]  | 1    | 1    | 1       | /         | 1      |
| HyperIQA [13]  | 1    | 1    | 1       | /         | -      |
| TReS [16]  | 1    | 1    | 1       | /         | 1      |
| DEIQT [34]   | 1    | 1    | 1       | /         | 1      |
| TempQT [52]  | -    | 1    | 1       | /         | -      |
| GlintIQA   | -    | 1    | 1       | /         | -      |

alization capability of models, which will be elaborated on in subsequent sections. The proposed dataset is constructed to address the content-limited issue of synthetic distorted datasets. Due to the inherent discrepancy between the distributions of synthetic and authentic distortions [12], the pre-trained GlintIQA\* model was not evaluated on authentic datasets.

3) *Statistical significant test*: Following the method in [56], we employed the F-test to assess the statistical significance of

TABLE V  
SROCC EVALUATION ACROSS SYNTHETIC DISTORTION DATASETS.

| Training<br>Testing | LIVE         |              | CSIQ         |              | TID2013      |              | Average      |
|---------------------|--------------|--------------|--------------|--------------|--------------|--------------|--------------|
|                     | CSIQ         | TID2013      | LIVE         | TID2013      | LIVE         | CSIQ         |              |
| DIIVINE [3]         | 0.553        | 0.487        | 0.794        | 0.372        | 0.716        | 0.555        | 0.580        |
| HOSA [54]           | 0.594        | 0.361        | 0.773        | 0.329        | 0.846        | 0.612        | 0.586        |
| BRISQUE [6]         | 0.562        | 0.358        | 0.847        | 0.454        | 0.774        | 0.586        | 0.597        |
| WaDIQaM [11]        | 0.704        | 0.462        | -            | -            | 0.817        | 0.690        | -            |
| HyperIQA [13]       | 0.744        | 0.583        | 0.905        | 0.554        | 0.856        | 0.692        | 0.722        |
| TReS [16]           | 0.761        | 0.534        | 0.939        | 0.543        | 0.888        | 0.708        | 0.729        |
| DB-CNN [12]         | 0.758        | 0.524        | 0.877        | 0.540        | 0.891        | 0.807        | 0.733        |
| VCRNet [55]         | 0.768        | 0.502        | 0.886        | 0.542        | 0.822        | 0.721        | 0.707        |
| Hu et al. [32]      | 0.769        | 0.584        | 0.924        | 0.554        | 0.881        | 0.736        | 0.741        |
| GlintIQA            | <b>0.797</b> | <b>0.664</b> | <b>0.945</b> | <b>0.596</b> | <b>0.936</b> | 0.749        | <b>0.781</b> |
| GlintIQA*           | <b>0.865</b> | <b>0.675</b> | <b>0.944</b> | <b>0.695</b> | <b>0.956</b> | <b>0.897</b> | <b>0.839</b> |

the proposed methods in comparison to competing approaches across diverse datasets. Experiments were conducted at a 95% confidence level to ensure the robustness and reliability of the results. The F-test results are presented in Table IV, where '1', '0', and '-' indicate that the model in the row is statistically superior to, inferior to, or indistinguishable from the model in the column, respectively. '-' denotes that performance data is unavailable for that dataset, precluding comparison. For the five authentic distortion datasets, GlintIQA demonstrates statistically significant superiority over DB-CNN, HyperIQA, and TReS. It shows comparable performance to TempQT on the SPAQ dataset while outperforming it on the remaining four datasets. Compared to DEIQT, GlintIQA underperforms on LIVEFB but performs better or comparably on the other datasets. On the five synthetic distortion datasets, GlintIQA\* was benchmarked against other methods and exhibited superior performance or was on par with the competitors. Overall, the proposed methods exhibit robust and consistent performance across both types of distortion datasets, underscoring their efficacy in addressing various types of image distortions.

### C. Comparison with BIQA Methods on Cross-dataset Testing

To rigorously evaluate the generalization abilities of BIQA models, we trained them on a complete database and subsequently assessed their performance on distinct, unseen databases. To ensure the reliability of results, each experiment was repeated ten times with randomized initializations, and the median of the resulting SROCC scores is presented. The experiments of our model were trained for 300 epochs and tested at 5 epoch intervals.

1) *Cross synthetic database evaluation:* Table V presents results for six cross-synthetic database tests. The proposed GlintIQA and GlintIQA\* models demonstrate exceptional performance across various cross-synthetic database tests, where GlintIQA achieves an average SROCC of 0.781, while GlintIQA\* achieves an even higher average SROCC of 0.839. In particular, GlintIQA surpasses Hu et al.'s method [32] by 3.64% and 13.70% when trained on LIVE and tested on CSIQ and TID2013, respectively. When trained on CSIQ, GlintIQA outperforms TReS by 0.64% on LIVE and the second-ranked method by 7.58% on TID2013. Trained on TID2013 and tested on LIVE, GlintIQA outperforms DB-CNN by 5.05%, and DB-CNN outperforms GlintIQA by 7.74% on CSIQ, attributed to

TABLE VI  
SROCC EVALUATION ACROSS AUTHENTIC DISTORTION DATASETS.

| Training<br>Testing | CLIVE        |              | KonIQ-10k    |              | BID          |              | Average      |
|---------------------|--------------|--------------|--------------|--------------|--------------|--------------|--------------|
|                     | BID          | KonIQ-10k    | BID          | CLIVE        | CLIVE        | KonIQ-10k    |              |
| DB-CNN [12]         | 0.762        | 0.754        | 0.816        | 0.755        | 0.725        | 0.724        | 0.756        |
| HyperIQA [13]       | 0.756        | <b>0.772</b> | 0.819        | 0.785        | 0.770        | 0.688        | 0.765        |
| REQA [31]           | 0.825        | 0.762        | 0.772        | <b>0.833</b> | 0.747        | 0.699        | 0.773        |
| TReS [16]           | <b>0.859</b> | 0.733        | 0.815        | 0.786        | 0.754        | 0.707        | 0.776        |
| DEIQT [34]          | 0.852        | 0.744        | <b>0.849</b> | 0.794        | <b>0.787</b> | <b>0.731</b> | <b>0.793</b> |
| GlintIQA            | <b>0.883</b> | <b>0.794</b> | <b>0.858</b> | <b>0.859</b> | <b>0.837</b> | <b>0.767</b> | <b>0.833</b> |

additional data used for pre-training. However, GlintIQA\* with extra pre-training data achieves an 11.30% improvement over DB-CNN.

Furthermore, GlintIQA\* demonstrates advancements in several other cross-dataset tests, such as an 8.53% improvement over GlintIQA when trained on LIVE and tested on CSIQ, and a remarkable 16.60% improvement when trained on CSIQ and tested on TID2013. The results highlight the effectiveness of our proposed dataset for enhancing model generalization by providing diverse image content for the model to learn distortion and quality variations. In addition, GlintIQA stands out even without pre-training, surpassing existing methods thanks to its dual focus on global and local features for capturing image distortions. Its combination of convolutional networks and ViT further bolsters its ability to learn and generalize effectively.

2) *Cross authentic database evaluation:* Table VI presents the performance of six cross-authentic dataset tests. The proposed GlintIQA demonstrates the best results across all six cross-authentic database tests. GlintIQA achieves the highest overall average performance, surpassing the second-ranked DEIQT by a significant 5.04%. When trained on CLIVE, GlintIQA excels on both BID and KonIQ-10k, outperforming TReS by 2.79% and HyperIQA by 2.85%, respectively. GlintIQA, when trained on KonIQ-10k, surpasses DEIQT by 1.06% on BID and REQA by 3.12% on CLIVE. Notably, GlintIQA achieves even more impressive gains on the relatively small-scale BID dataset, outperforming the second-ranked methods in CLIVE and KonIQ-10k by 6.35% and 4.92%, respectively. These results provide convincing evidence of GlintIQA's superior generalization capabilities, highlighting its ability to adapt effectively to diverse image quality assessment scenarios.

### D. Ablation Study

1) *Model components:* To validate the effectiveness of individual components in the proposed GlintIQA, we conduct two types of ablation studies: evaluations on a single dataset and across-dataset tests. The model configurations are illustrated in Fig. 8 (omitting feature concatenation, reshaping, and flattening operations for clarity). The structures are described as follows: **a**) Utilize CLFE module to extract local multi-scale features and perform regression using MLP on the embedded features. **b**) Employ VGFE module to extract global multi-scale features and regress them with MLP. **c**) Jointly leverage both CLFE and VGFE modules to extract local and global multi-scale features followed by regression. **d**) The proposed

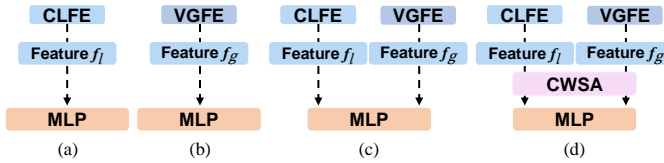


Fig. 8. Schematic diagrams of different model structures.

TABLE VII  
ABLATION STUDIES OF DIFFERENT COMPONENTS OF GLINTIQA ON INDIVIDUAL DATASET TESTS.

| Setting           | LIVE   |        | CLIVE  |        | Average |        |
|-------------------|--------|--------|--------|--------|---------|--------|
|                   | SROCC  | PLCC   | SROCC  | PLCC   | SROCC   | PLCC   |
| a) CLFE           | 0.9629 | 0.9661 | 0.8289 | 0.8323 | 0.8959  | -      |
| b) VGFE           | 0.9720 | 0.9753 | 0.8810 | 0.9050 | 0.9265  | +3.42% |
| c) CLFE+VGFE      | 0.9733 | 0.9767 | 0.8856 | 0.9061 | 0.9295  | +3.75% |
| d) CLFE+VGFE+CWSA | 0.9744 | 0.9769 | 0.8883 | 0.9058 | 0.9314  | +3.96% |
| e) Proposed       | 0.9756 | 0.9797 | 0.8907 | 0.9072 | 0.9332  | +4.16% |

TABLE VIII  
ABLATION STUDIES OF DIFFERENT COMPONENTS OF GLINTIQA ON CROSS-DATASET TESTS, WHERE THE RESULTS ARE SROCC VALUES.

| Setting           | LIVE   |         | CLIVE  |           | Average |        |
|-------------------|--------|---------|--------|-----------|---------|--------|
|                   | CSIQ   | TID2013 | BID    | KonIQ-10k | SROCC   | PLCC   |
| a) CLFE           | 0.7572 | 0.5792  | 0.8374 | 0.7306    | 0.7261  | -      |
| b) VGFE           | 0.7890 | 0.6366  | 0.8691 | 0.7687    | 0.7659  | +5.48% |
| c) CLFE+VGFE      | 0.7772 | 0.6417  | 0.8738 | 0.7798    | 0.7681  | +5.78% |
| d) CLFE+VGFE+CWSA | 0.7868 | 0.6545  | 0.8780 | 0.7723    | 0.7729  | +6.45% |
| e) Proposed       | 0.7973 | 0.6637  | 0.8831 | 0.7938    | 0.7845  | +8.04% |

model sans the SEM modules. **e)** The model in its complete form, as shown in Fig. 1.

Based on the performance comparisons in Tables VII and VIII, where the **blue**-highlighted values signify performance gains achieved by other model configurations relative to model a, several key observations can be made: **1)** The model b employing VGFE, outperforms the model utilizing LFE by 3.42% in terms of SROCC on individual datasets, and 5.48% on cross-dataset evaluations. The results indicate that global features are capable of capturing more comprehensive information pertaining to image quality in comparison to local features. **2)** Model c, which combines CLFE and VGFE, achieves consistent enhancement over model a, with a 3.75% gain in SROCC on individual datasets and a 5.78% gain on cross-dataset evaluations. These results demonstrate the complementary effects of local and global features. **3)** Model d, which incorporates CWSA, attains a 3.96% improvement in SROCC on individual datasets and a 6.45% improvement on cross-dataset evaluations. This outcome suggests that CWSA can facilitate the model's ability to better concentrate on the salient features of images. **4)** Model e, which combines CWSA and SEM, achieves the best performance, with a 4.16% increment in SROCC on individual datasets and an 8.04% increment on cross-dataset evaluations. This suggests that the interactive stacking of CWSA and SEM is highly effective in improving the integration and utilization of multi-scale features, allowing an accurate evaluation of image quality.

**2) The proposed dataset:** To validate the effectiveness of our proposed dataset, besides the initial validations in Tables III and V, we also conducted cross-dataset tests on KADID-10k, pitting GlintIQA against two other BIQA models, i.e., TReS and DEIQT. Their experimental results were

TABLE IX  
ABLATION STUDY OF THE PROPOSED DATASET ON CROSS-DATABASE TESTS AND COMPARISON OF BIQA MODELS.

| Testing    | LIVE          |               | CSIQ          |               | Average       |               |
|------------|---------------|---------------|---------------|---------------|---------------|---------------|
|            | SROCC         | PLCC          | SROCC         | PLCC          | SROCC         | PLCC          |
| DEIQT [34] | 0.9071        | 0.8844        | 0.7942        | 0.8021        | 0.8507        | 0.8433        |
| TReS [16]  | 0.9195        | 0.9071        | 0.7932        | 0.8250        | 0.8563        | 0.8661        |
| GlintIQA   | <b>0.9389</b> | <b>0.9158</b> | <b>0.8097</b> | <b>0.8276</b> | <b>0.8743</b> | <b>0.8717</b> |
| GlintIQA*  | <b>0.9503</b> | <b>0.9305</b> | <b>0.8931</b> | <b>0.9127</b> | <b>0.9217</b> | <b>0.9216</b> |

replicated utilizing the publicly accessible code under the same training and test sets. As shown in Table IX, the results show that even without pretraining, GlintIQA confidently surpasses both TReS and DEIQT in these evaluations. Furthermore, the pretrained GlintIQA\* amplifies these advantages, boasting average SROCC and PLCC improvements of 5.42% and 5.72% over its non-pre-trained counterpart, GlintIQA. Notably, our proposed dataset is constructed using the labels of KADID-10k. The performance gains achieved by the pre-trained model can be attributed to two key factors: our dataset sufficiently increases the diversity of image content and the effectiveness of the image quality label annotation method.

To facilitate visual comparison, we additionally conducted a group maximum differentiation (gMAD) competition [57] between GlintIQA and GlintIQA\* on Waterloo database [58]. In the evaluation, a defender model categorizes image quality into six levels, while an attacker model aims to expose its weaknesses by identifying image pairs with significant quality discrepancies within those levels. Specifically, the attacker selects images that the defender model rates similarly but that the attacker model perceives as having a large quality gap. This approach reveals differences in quality perception between models. Fig. 9 shows the gMAD competition between GlintIQA and pretrained GlintIQA\*. When fixed as the defender GlintIQA, GlintIQA\* successfully recognizes perceptually different image pairs, whereas the attack by GlintIQA results in image pairs with negligible quality differences. This verifies that pretrained GlintIQA\* can further enhance model generalizability, solidifying the validity of our proposed dataset.

## VI. CONCLUSION

In this study, we have enhanced the effectiveness and robustness of BIQA by optimizing the network architecture and augmenting the training data. We proposed a novel BIQA model GlintIQA that leverages the synergy between CNNs and ViTs to extract complementary local and global multi-grained features. This hybrid architecture mitigates patch-level information loss and inductive bias limitations inherent in ViTs. GlintIQA employs a progressive integration strategy with interactive stacking channel-wise self-attention and spatial enhancement modules, efficiently handling diverse features across both channels and spatial dimensions. Furthermore, to overcome the issue of limited content variation in synthetic distortion datasets, we propose a novel content-guided method for automatic image quality labeling based on subjective

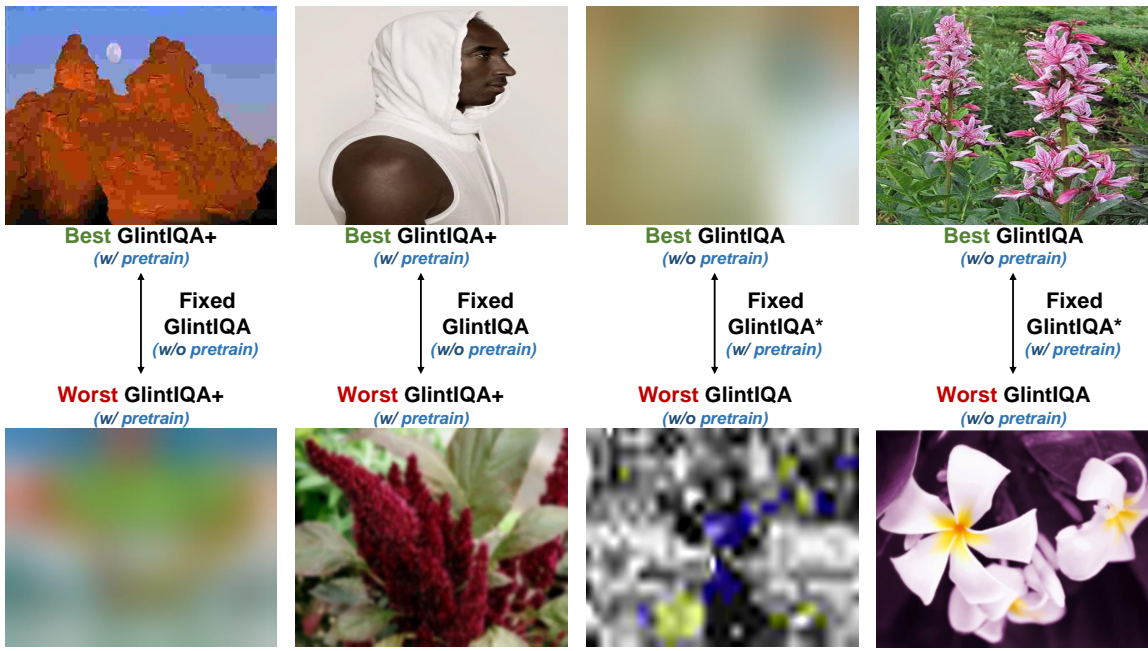


Fig. 9. Results of gMAD competition between GlintIQA and GlintIQA\*. The left two columns show fixed GlintIQA at low- and high-quality levels, respectively. The right two columns show fixed GlintIQA\* at low- and high-quality levels, respectively.

quality scores. The proposed content-guided labeling method plays a pivotal role in significantly diversifying and enriching the training data, resulting in a substantial boost in model generalization ability. The innovative architecture of GlintIQA, combined with the proposed content-driven dataset, leads to a significant improvement in BIQA performance, as evidenced by extensive single-dataset and cross-dataset evaluations.

## REFERENCES

- [1] W. Lin and C.-C. J. Kuo, “Perceptual visual quality metrics: A survey,” *Journal of visual communication and image representation*, vol. 22, no. 4, pp. 297–312, 2011.
- [2] A. K. Moorthy and A. C. Bovik, “A two-step framework for constructing blind image quality indices,” vol. 17, no. 5, pp. 513–516, 2010.
- [3] Moorthy, Anush Krishna and Bovik, Alan Conrad, “Blind image quality assessment: From natural scene statistics to perceptual quality,” vol. 20, no. 12, pp. 3350–3364, 2011.
- [4] M. A. Saad, A. C. Bovik, and C. Charrier, “Blind image quality assessment: A natural scene statistics approach in the dct domain,” vol. 21, no. 8, pp. 3339–3352, 2012.
- [5] L. Zhang, L. Zhang, and A. C. Bovik, “A feature-enriched completely blind image quality evaluator,” vol. 24, no. 8, pp. 2579–2591, 2015.
- [6] A. Mittal, A. K. Moorthy, and A. C. Bovik, “No-reference image quality assessment in the spatial domain,” vol. 21, no. 12, pp. 4695–4708, 2012.
- [7] L. Kang, P. Ye, Y. Li, and D. Doermann, “Convolutional neural networks for no-reference image quality assessment,” 2014, pp. 1733–1740.
- [8] J. Kim, A.-D. Nguyen, and S. Lee, “Deep cnn-based blind image quality predictor,” vol. 30, no. 1, pp. 11–24, 2019.
- [9] K. Ma, W. Liu, K. Zhang, Z. Duanmu, Z. Wang, and W. Zuo, “End-to-end blind image quality assessment using deep neural networks,” vol. 27, no. 3, pp. 1202–1213, 2018.
- [10] X. Liu, J. Van De Weijer, and A. D. Bagdanov, “Rankiqa: Learning from rankings for no-reference image quality assessment,” 2017, pp. 1040–1049.
- [11] S. Bosse, D. Maniry, K.-R. Müller, T. Wiegand, and W. Samek, “Deep neural networks for no-reference and full-reference image quality assessment,” vol. 27, no. 1, pp. 206–219, 2018.
- [12] W. Zhang, K. Ma, J. Yan, D. Deng, and Z. Wang, “Blind image quality assessment using a deep bilinear convolutional neural network,” vol. 30, no. 1, pp. 36–47, 2020.
- [13] S. Su, Q. Yan, Y. Zhu, C. Zhang, X. Ge, J. Sun, and Y. Zhang, “Blindly assess image quality in the wild guided by a self-adaptive hyper network,” 2020, pp. 3664–3673.
- [14] F.-Z. Ou, Y.-G. Wang, J. Li, G. Zhu, and S. Kwong, “A novel rank learning based no-reference image quality assessment method,” pp. 1–1, 2021.
- [15] S. Lao, Y. Gong, S. Shi, S. Yang, T. Wu, J. Wang, W. Xia, and Y. Yang, “Attentions help cnns see better: Attention-based hybrid image quality assessment network,” June 2022, pp. 1140–1149.
- [16] S. A. Golestaneh, S. Dadsetan, and K. M. Kitani, “No-reference image quality assessment via transformers, relative ranking, and self-consistency,” in *Proceedings of the IEEE/CVF Winter Conference on Applications of Computer Vision*, 2022, pp. 3209–3218.
- [17] J. You and J. Korhonen, “Transformer for image quality assessment,” 2021, pp. 1389–1393.
- [18] A. Dosovitskiy, L. Beyer, A. Kolesnikov, D. Weissenborn, X. Zhai, T. Unterthiner, M. Dehghani, M. Minderer, G. Heigold, S. Gelly *et al.*, “An image is worth 16x16 words: Transformers for image recognition at scale,” 2020.
- [19] S. d’Ascoli, H. Touvron, M. L. Leavitt, A. S. Morcos, G. Biroli, and L. Sagun, “Convit: Improving vision transformers with soft convolutional inductive biases,” *PMLR*, 2021, pp. 2286–2296.
- [20] H. Bao, L. Dong, S. Piao, and F. Wei, “Beit: Bert pre-training of image transformers,” 2021.
- [21] Z. Dai, H. Liu, Q. V. Le, and M. Tan, “Coatnet: Marrying convolution and attention for all data sizes,” vol. 34, pp. 3965–3977, 2021.
- [22] H. Sheikh, M. Sabir, and A. Bovik, “A statistical evaluation of recent full reference image quality assessment algorithms,” vol. 15, no. 11, pp. 3440–3451, 2006.
- [23] N. Ponomarenko, L. Jin, O. Ieremeiev, V. Lukin, K. Egiazarian, J. Astola, B. Vozel, K. Chehdi, M. Carli, F. Battisti *et al.*, “Image database tid2013: Peculiarities, results and perspectives,” *Signal processing: Image communication*, vol. 30, pp. 57–77, 2015.
- [24] H. Lin, V. Hosu, and D. Saupe, “Kadid-10k: A large-scale artificially distorted iqas database,” in *2019 Eleventh International Conference on Quality of Multimedia Experience (QoMEX)*, 2019, pp. 1–3.
- [25] T.-J. Liu, W. Lin, and C.-C. J. Kuo, “Image quality assessment using multi-method fusion,” *IEEE Transactions on Image Processing*, vol. 22, no. 5, pp. 1793–1807, 2013.
- [26] Q. Yan, D. Gong, and Y. Zhang, “Two-stream convolutional networks for blind image quality assessment,” vol. 28, no. 5, pp. 2200–2211, 2019.
- [27] J. Ma, J. Wu, L. Li, W. Dong, X. Xie, G. Shi, and W. Lin, “Blind image quality assessment with active inference,” vol. 30, pp. 3650–3663, 2021.

[28] J. Wu, J. Ma, F. Liang, W. Dong, G. Shi, and W. Lin, "End-to-end blind image quality prediction with cascaded deep neural network," vol. 29, pp. 7414–7426, 2020.

[29] M. D. Zeiler and R. Fergus, "Visualizing and understanding convolutional networks," in *Computer Vision–ECCV 2014: 13th European Conference, Zurich, Switzerland, September 6–12, 2014, Proceedings, Part I 13*. Springer, 2014, pp. 818–833.

[30] M. Zhu, G. Hou, X. Chen, J. Xie, H. Lu, and J. Che, "Saliency-guided transformer network combined with local embedding for no-reference image quality assessment," October 2021, pp. 1953–1962.

[31] B. Li and F. Huo, "Reqa: Coarse-to-fine assessment of image quality to alleviate the range effect," *Journal of Visual Communication and Image Representation*, vol. 98, p. 104043, 2024.

[32] B. Hu, G. Zhu, L. Li, J. Gan, W. Li, and X. Gao, "Blind image quality index with cross-domain interaction and cross-scale integration," pp. 1–11, 2023.

[33] J. Wang, H. Fan, X. Hou, Y. Xu, T. Li, X. Lu, and L. Fu, "Mstriq: No reference image quality assessment based on swin transformer with multi-stage fusion," in *Proceedings of the IEEE/CVF Conference on Computer Vision and Pattern Recognition*, 2022, pp. 1269–1278.

[34] G. Qin, R. Hu, Y. Liu, X. Zheng, H. Liu, X. Li, and Y. Zhang, "Data-efficient image quality assessment with attention-panel decoder," in *Proceedings of the AAAI Conference on Artificial Intelligence (AAAI)*, 2023.

[35] J. Kim and S. Lee, "Fully deep blind image quality predictor," vol. 11, no. 1, pp. 206–220, 2017.

[36] J. Gu, G. Meng, C. Da, S. Xiang, and C. Pan, "No-reference image quality assessment with reinforcement recursive list-wise ranking," vol. 33, no. 01, 2019, pp. 8336–8343.

[37] L. Zhang, Y. Shen, and H. Li, "Vsi: A visual saliency-induced index for perceptual image quality assessment," vol. 23, no. 10, pp. 4270–4281, 2014.

[38] K. He, X. Zhang, S. Ren, and J. Sun, "Deep residual learning for image recognition," 2016, pp. 770–778.

[39] S. W. Zamir, A. Arora, S. Khan, M. Hayat, F. S. Khan, and M.-H. Yang, "Restormer: Efficient transformer for high-resolution image restoration," 2022, pp. 5728–5739.

[40] X. Wang, J. Xiong, H. Gao, and W. Lin, "Regression-free blind image quality assessment," *arXiv preprint arXiv:2307.09279*, 2023.

[41] Z. Wang, A. Bovik, H. Sheikh, and E. Simoncelli, "Image quality assessment: from error visibility to structural similarity," vol. 13, no. 4, pp. 600–612, 2004.

[42] L. Zhang, L. Zhang, X. Mou, and D. Zhang, "Fsim: A feature similarity index for image quality assessment," vol. 20, no. 8, pp. 2378–2386, 2011.

[43] E. C. Larson and D. M. Chandler, "Most apparent distortion: full-reference image quality assessment and the role of strategy," *Journal of electronic imaging*, vol. 19, no. 1, p. 011006, 2010.

[44] D. Jayaraman, A. Mittal, A. K. Moorthy, and A. C. Bovik, "Objective quality assessment of multiply distorted images," in *2012 Conference Record of the Forty Sixth Asilomar Conference on Signals, Systems and Computers (ASILOMAR)*, 2012, pp. 1693–1697.

[45] A. Ciancio, A. L. N. T. Targino da Costa, E. A. B. da Silva, A. Said, R. Samadani, and P. Obrador, "No-reference blur assessment of digital pictures based on multifeature classifiers," vol. 20, no. 1, pp. 64–75, 2011.

[46] D. Ghadiyaram and A. C. Bovik, "Massive online crowdsourced study of subjective and objective picture quality," vol. 25, no. 1, pp. 372–387, 2016.

[47] V. Hosu, H. Lin, T. Sziranyi, and D. Saupe, "Koniq-10k: An ecologically valid database for deep learning of blind image quality assessment," vol. 29, pp. 4041–4056, 2020.

[48] Y. Fang, H. Zhu, Y. Zeng, K. Ma, and Z. Wang, "Perceptual quality assessment of smartphone photography," 2020, pp. 3674–3683.

[49] Z. Ying, H. Niu, P. Gupta, D. Mahajan, D. Ghadiyaram, and A. Bovik, "From patches to pictures (paq-2-piq): Mapping the perceptual space of picture quality," 2020, pp. 3572–3582.

[50] D. Li, T. Jiang, W. Lin, and M. Jiang, "Which has better visual quality: The clear blue sky or a blurry animal?" vol. 21, no. 5, pp. 1221–1234, 2019.

[51] J. Ke, Q. Wang, Y. Wang, P. Milanfar, and F. Yang, "Musiq: Multi-scale image quality transformer," in *Proceedings of the IEEE/CVF International Conference on Computer Vision*, 2021, pp. 5148–5157.

[52] J. Shi, P. Gao, and A. Smolic, "Blind image quality assessment via transformer predicted error map and perceptual quality token," *IEEE Transactions on Multimedia*, vol. 26, pp. 4641–4651, 2024.

[53] S. Yang, Q. Jiang, W. Lin, and Y. Wang, "Sgdnet: An end-to-end saliency-guided deep neural network for no-reference image quality assessment," 2019, pp. 1383–1391.

[54] J. Xu, P. Ye, Q. Li, H. Du, Y. Liu, and D. Doermann, "Blind image quality assessment based on high order statistics aggregation," vol. 25, no. 9, pp. 4444–4457, 2016.

[55] Z. Pan, F. Yuan, J. Lei, Y. Fang, X. Shao, and S. Kwong, "Vcrnet: Visual compensation restoration network for no-reference image quality assessment," vol. 31, pp. 1613–1627, 2022.

[56] L. Li, D. Wu, J. Wu, H. Li, W. Lin, and A. C. Kot, "Image sharpness assessment by sparse representation," *IEEE Transactions on Multimedia*, vol. 18, no. 6, pp. 1085–1097, 2016.

[57] K. Ma, Q. Wu, Z. Wang, Z. Duanmu, H. Yong, H. Li, and L. Zhang, "Group mad competition - a new methodology to compare objective image quality models," June 2016.

[58] K. Ma, Z. Duanmu, Q. Wu, Z. Wang, H. Yong, H. Li, and L. Zhang, "Waterloo exploration database: New challenges for image quality assessment models," vol. 26, no. 2, pp. 1004–1016, 2017.